Cytometry
PART A
Journal of the International Society for Advancement of Cytometry

Biolens Behavior of RBCs Under Optically-Induced Mechanical Stress

Francesco Merola,[1]* Álvaro Barroso,[2] Lisa Miccio,[1] Pasquale Memmolo,[1] Martina Mugnano,[1] Pietro Ferraro,[1] Cornelia Denz[2]

[1]Istituto di Scienze Applicate e Sistemi Intelligenti del CNR (ISASI-CNR), Via Campi Flegrei 34, Pozzuoli, 80078, Italy

[2]Institute of Applied Physics, University of Muenster, Corrensstrasse 2-4, Muenster, 48149, Germany

Received 27 October 2016; Revised 22 February 2017; Accepted 25 February 2017

Additional Supporting Information may be found in the online version of this article.

*Correspondence to: Francesco Merola, Via Campi Flegrei 34, 80078 Pozzuoli (NA), Italy. E-mail: f.merola@isasi.cnr.it

F. Merola, A. Barroso, and L. Miccio contributed equally to this work.

Published online 00 Month 2017 in Wiley Online Library (wileyonlinelibrary.com)

DOI: 10.1002/cyto.a.23085

• **Abstract**

In this work, the optical behavior of Red Blood Cells (RBCs) under an optically-induced mechanical stress was studied. Exploiting the new findings concerning the optical lens-like behavior of RBCs, the variations of the wavefront refracted by optically-deformed RBCs were further investigated. Experimental analysis have been performed through the combination of digital holography and numerical analysis based on Zernike polynomials, while the biological lens is deformed under the action of multiple dynamic optical tweezers. Detailed wavefront analysis provides comprehensive information about the aberrations induced by the applied mechanical stress. By this approach it was shown that the optical properties of RBCs in their discocyte form can be affected in a different way depending on the geometry of the deformation. In analogy to classical optical testing procedures, optical parameters can be correlated to a particular mechanical deformation. This could open new routes for analyzing cell elasticity by examining optical parameters instead of direct but with low resolution strain analysis, thanks to the high sensitivity of the interferometric tool. Future application of this approach could lead to early detection and diagnosis of blood diseases through a single-step wavefront analysis for evaluating different cells elasticity. © 2017 International Society for Advancement of Cytometry

• **Key terms**

red blood cells; digital holography; optical tweezers; biolens effect; cell elasticity; Zernike polynomials; lens aberration

Introduction

Red blood cells (RBCs) are responsible for the exchange of respiratory gases at tissues level. Transportation and delivering of these gases through the whole body is possible through the extensive deformations of RBCs when they get through the smallest capillaries of the vascular system. The great deformability of RBCs can be altered by various pathological conditions and, at the same time, abnormal RBC deformability can lead to pathological implications. For example, depending on the storage conditions, RBCs can undergo changes in deformability, a critical parameter of storage lesion, while a close association between RBC storage and complications of blood transfusion has been demonstrated (1–3). Similarly, the morphology of cells is of key importance for aging issues, deformability/elasticity analysis and diagnostic purposes. Thus, alterations of both mechanical and morphological properties in RBCs have been regarded as direct indicators of blood quality (4,5) and, for these reasons, are subject of intense and worldwide studies (6–8). The development of non-invasive methods that enable the identification of morphological and biomechanical variations of RBCs is thus of utmost scientific and medical interest.

On the one hand, a first main requisite for the investigation of human diseases based on the cellular biomechanics is a method to exert non-destructive forces on

ISAC
International Society for Advancement of Cytometry

the inner or outer cell membrane (9). Several methods have been developed for investigating the difference of the mechanical properties of healthy and sick RBCs. Common techniques for addressing this purpose are based on particular microfluidic channels (10–13), and on various electrical/optical techniques, such as atomic force microscopy (4,14), dielectrophoresis (15), and optical trapping techniques (16–21). For example, parachute and slipper shapes are produced, respectively, in small and large one-dimensional microchannels (22), while optically-induced deformation using the optical stretcher is typically limited to cell elongation along a defined direction due to the applied antipodal stretching forces (19,23). Nevertheless, these approaches lack flexibility and re-configurability with respect to different cell shape deformations. In this respect, optical tweezers (OT) stand out due to their high precision to trap and manipulate transparent microparticles, as living cells, near the focus spot of a tightly focused laser beam (24). Most popular applications of OT concern the confinement of single cells to organize, assemble, locate, sort, and modify them. Due to their versatility to deform cells with forces in the pN range, OT have been employed as an efficient and contact-less apparatus for studying the mechanical properties of isolated biological systems (25–27). Moreover, holographic optical tweezers (HOT) extend further the capabilities of conventional OT through the generation of multiple optical traps by modulating the phase front of the trapping laser beam (28). The optical traps can be controlled individually in three-dimensions allowing multiplexed force measurements on living cells through the control of several optically-driven microspheres at the same time (29), and through the manipulation of other microprobes with a more complex geometry (30–32).

On the other hand, a second crucial issue is to study the cell response during the manipulation and deformation upon an external stimuli. Among the established techniques, simultaneous quantitative imaging provides additional key information on the morphological cellular properties, and thus a closer clue about the cellular pathological state. Since the same objective lens that is used for optical trapping is typically employed for observation of the sample, HOT permit a readily combination with many microscopy techniques. Beside the straightforward use of bright field microscopy to analyze shape changes during deformation (33), various imaging and spectroscopy techniques have been proposed in combination with HOT during optical manipulation of RBCs, as for example, fluorescence microscopy and Raman spectroscopy (18,34). In particular, the combination of digital holographic microscopy (DHM) with HOT represents a state-of-the-art strategy for simultaneous single cell manipulation and quantitative phase imaging of the cell morphology. DHM is a label-free technique that retrieves numerically the complete information, that is, amplitude and phase, of a complex object wave that propagates through a transparent sample. Importantly, this quantitative phase data allows determination of the refractive index and thickness of cells (35–38). Furthermore, stacking of numerically refocused amplitude images from the image plane to different planes along the propagation direction can be used as a simple strategy to study the scattered light intensity in the near-field close to the particle (39). So far, the universality of the technique has been applied for inanimate silica and polystyrene microspheres as well as for various types of living organisms as eukaryotes, bacteria, diatoms, erythrocytes, yeast and cancer cells (38,40–43).

By controlling the cell orientation to determine the RBC morphology and by analyzing their scattered light, DHM + HOT have led to the recent discovery that RBCs behave efficiently as adaptive optofluidic microlenses (44). In fact, a RBC can be seen as a 3D envelope filled by a sort of uniform liquid showing optical focusing properties. In their discocyte form, the inner part, that is, the central region with a double concavity, provides a negative focal length, while the edges behave as a sort of toroid lens having a positive focal length. By changing the chemical buffer in order to induce osmotic cell swelling, RBCs easily vary their shape to spherocytes, which lack the central concavity, and change consequently their optical properties. In this way, the change from disk volume to a sphere leads to changes of the focal length from negative to positive values. In analogy to well-established wavefront analysis based on Zernike polynomials which is commonly adopted for testing optical systems with extremely high precision, one can argue that a RBC under mechanical stress can behave as a lens with specific aberrations, thus distorting the transmitted light. In particular, the focal properties of discocytes correspond to the contributions of Zernike coefficients of order 4 and 12, that is, respectively, focus shift and third-order spherical aberrations, while other terms are negligible. Meanwhile spherocytes can be described essentially only by a focus-shift term (44). This new finding opens the route to a different kind of analysis of the biomechanical properties of RBCs. For example, accurate analysis of the wavefront could in principle allow to retrieve the three-dimensional deformations experienced by RBCs under the action of an external stress. In this sense, DHM has proved to be a perfect tool for analyzing the aberrations/deformations of microlenses (45,46).

Here, we exploit the unique features of DHM + HOT for a deep investigation on wavefront diffracted by RBCs, which varies by applying a mechanical stress through multiple HOTs probes. Variations of the focusing properties of HOT-deformed RBC microlenses are investigated for two mechanical configurations and evaluated by a wavefront Zernike analysis. This study presents for the first time the use of HOTs to induce changes in the transmitted wavefront of a RBC and to classify and quantify the corresponding aberrations. It can constitute a significant know-how base for further understanding of the mechano-biological behavior of RBCs. Moreover, the reported results allow to verify how HOTs can change optical parameters of this biological lens for future applications as imaging element.

Materials and Methods

Optical Setup

For optical trapping a Neodymium-doped Yttrium Orthovanadate (Nd:YVO4) laser operating at a wavelength

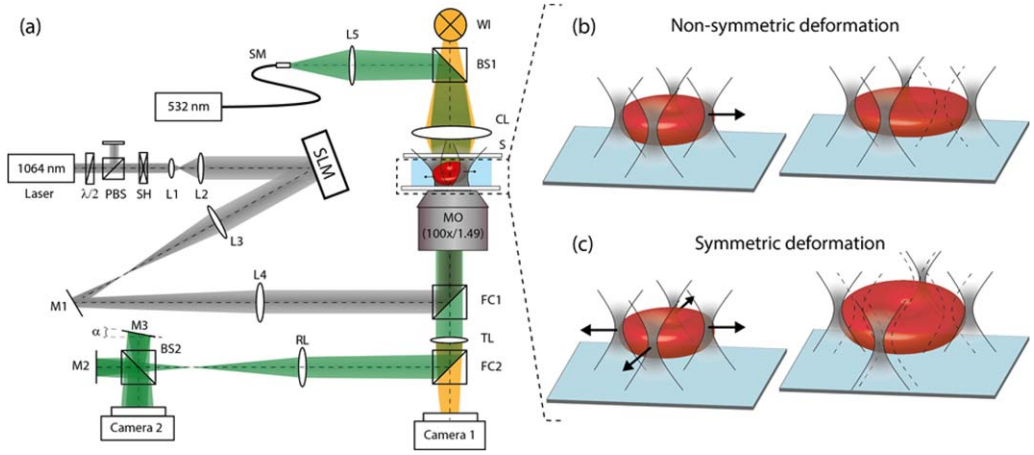

Figure 1. (a) Schematic of the combined DHM and HOT workstation used holographic optical stretching and quantitative phase imaging of RBCs. Optical elements: $\lambda/2$: rotatable half wave plate, PBS: polarizing beam splitter, SH: shutter, L: lens, SLM: spatial light modulator, M: mirror, FC: filter cube, WS: white light source, SM: single mode optical fiber, BS: non-polarizing beam splitter, CL: condenser lens, TL: tube lens, RL relay lens. (b, c) Schematic of the configuration of the optical traps for performing deformation of a single RBC in a (b) non-symmetrical and (c) symmetrical way. [Color figure can be viewed at wileyonlinelibrary.com]

$\lambda = 1{,}064$ nm and a maximum output power $P = 2.5$ W was used. The laser power was adjusted to 300 mW (measured at the entrance of the inverted microscope) with a half-wave plate and a polarizing beam splitter (PBS) in order to have a compromise between sufficiently high trapping forces and low photodamage on the biological specimen. This has been preliminarily tested by using different laser powers, as well as we confirmed that no damage to the cell was produced during the trapping experiments by monitoring the state of the cell under the microscope in real time. The light of the laser was expanded via a telescope (lenses L1 and L2) in order to illuminate adequately the surface of a spatial light modulator (SLM) (Pluto phase-only, 1,920 × 1,080 pixels, Holoeye Berlin, Germany). The SLM was set at a conjugated plane of the back focal plane of the microscope objective using the appropriate relay optics (lenses L3 and L4) in a double 2-f setup. In order to generate multiple dynamic optical traps in the specimen plane, the light beam was modulated with the SLM by means of computer-generated digital holograms using a software originally developed at the University of Glasgow, Scotland (47). The optical manipulation and stretching of the RBCs was observed by bright field imaging and quantitative phase imaging with DHM. For this purpose, the coherent light of a frequency-doubled neodymium-doped yttrium aluminum garnet (Nd:YAG) laser ($\lambda = 532$ nm) is introduced into the white light illumination path of the inverted microscope using a single mode (SM) optical fiber and a non-polarizing beam splitter (BS1). The microscope condenser lens (CL) and a lens (L5) were adjusted to provide suitable Koehler-like illumination. The microscope objective, a tube lens (TL) and a relay lens (RL) were used to magnify the sample (S), while a self-interference setup (formed by mirrors M3, M4 and a 50:50 beams splitter BS2) was adapted to one of the camera ports of the inverted microscope for creation and recording of the digital holograms. In order to produce suitable off-axis digital holograms, mirror M3 was tilted by a small angle α in such a way that an area of the sample that contains no object is superposed with the image of the specimen (48). The resulting interference pattern was imaged and recorded as a digital hologram by a second camera (Camera 2) (Imaging Source DMK 41BU02) and transferred to a computer for posterior numerical reconstruction. The numerical reconstruction of the digitally recorded holograms was performed by the standard algorithms as described in Refs. 49 and (50).

Sample Preparation

Healthy blood was collected from a healthy donor, who gave informed consent. The sample was prepared as follows: approximately 3 mL of heparinized whole blood was withdrawn into a hematocrit tube and pipetted when blood was clearly separated into its component parts (plasma, buffy coat and RBCs at the bottom of the centrifuge tube). About 1 μL of blood was diluted into 1,000 μL of phosphate-buffered saline. Then, 50 μL of this sample was diluted again with 500 μL of a solution of plasma (previously filtered with a 0.45-μm pore size syringe filter) and phosphate-buffered saline (concentration 2:10). Finally, 50 μL of the resulting dilution was pipetted and used to fill by capillarity the volume between two thin microscope slides. The prepared dilution sample was used within no longer than two days. For the measurement, only RBCs that showed a defined and clear discocyte shape were chosen.

Results and Discussion

For simultaneous three dimensional optical manipulation and quantitative phase imaging of single RBCs, a HOT system and a modular self-interference DHM setup were implemented on a commercial inverted microscope (Eclipse Ti, Nikon). A high numerical aperture microscope objective (Nikon Apo TIRF, 100×/1.49 oil-immersion) was used for both imaging and optical manipulation of the biological sample. Figure 1 depicts a schematic of the multimodal

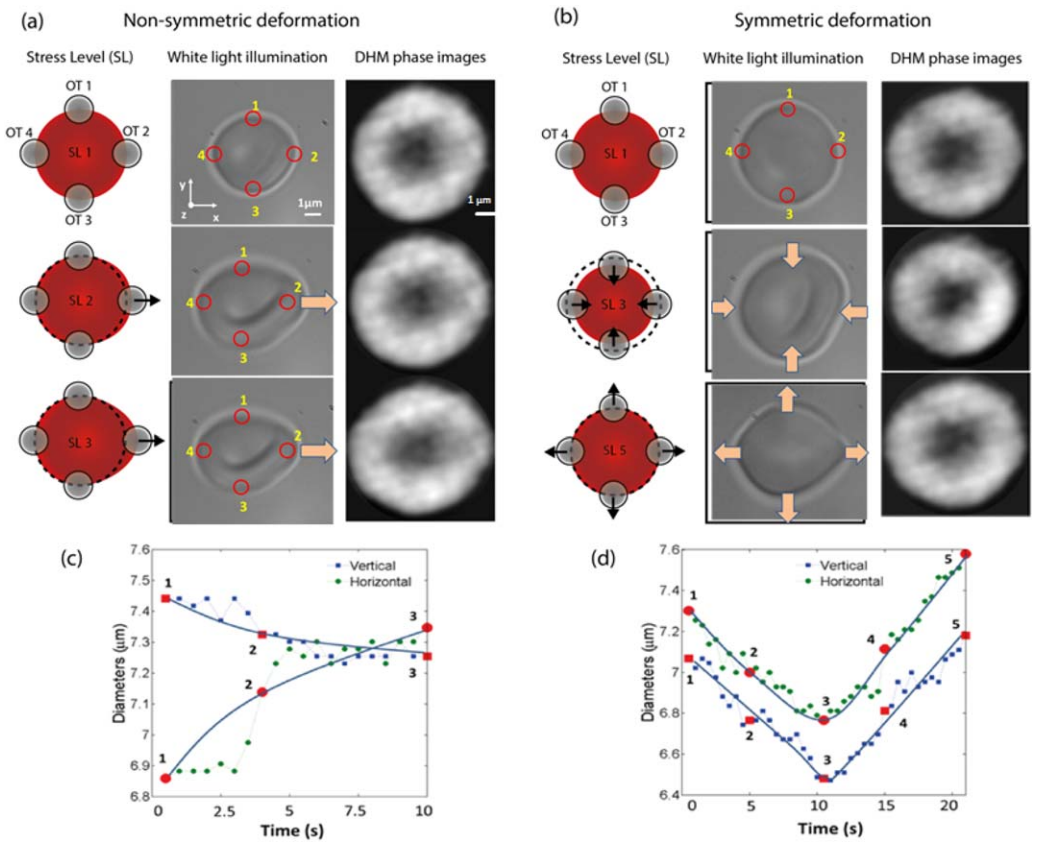

Figure 2. (a, b) Schematic of the optical traps configuration, DHM phase images of HOT-deformed discocytes during (a) non-symmetric and (b) symmetrical deformation. (c, d) Variation of RBC diameter during time, along vertical (squares) and horizontal (circles) directions. The numbers correspond to the stress level (SL) that are analyzed in more detail in Figures 3 and 4, while the continuous lines are just a guide for the eye. [Color figure can be viewed at wileyonlinelibrary.com]

holographic workstation that was used to perform the experiments (more details in "Materials and Methods" section). The principles of the HOT and DHM systems are described in detail in Refs. 51 and 52, respectively.

Firstly, in order to avoid the inherent orientation in an optical trap of RBCs, which align in direction of the light propagation (z-axis) (53), we generated multiple spots to rotate and orient the cell parallel to the x–y plane. Once the cell was aligned perpendicular to the optical axis, only four optical traps were utilized as anchored points at discrete locations to induce a controllable deformation of the cell. In particular, we tested the response of RBCs and their focusing properties under two different conditions. In the first case, we steered one of the four traps along the x-axis, while the other three traps remained at a fixed position, which induced a *non-symmetric* cell *deformation* along this direction. In the second case, a *symmetrical deformation* was addressed by squeezing and stretching the cell using four traps at the same time (Fig. 1c). Choosing between symmetric and asymmetric deformation is one of the versatility advantages that is intrinsic for HOT experiments compared with other microfluidic techniques which enable limited geometries of deformation. The manipulation of the RBCs was observed both under bright field microscope and by quantitative DHM phase contrast. Figure 2 shows a schematic of the optical trapping procedure for deformation of the cells, as well as the corresponding bright-field and quantitative phase microscopy (QPM) images before and after RBC deformation. The first quantitative evaluation of the optically-induced deformation is performed in terms of diameter changes measured on the QPM images; two graphs of the diameter variation during time corresponding to the two different deformation modes are displayed in Figures 2c and 2d. The complete image sequence of the deformation process corresponding to the phase map images of Figure 2 are shown in Supporting Information Movies 1 and 2. Noteworthy, slight variations of the RBC diameter during HOT-induced deformation are detected with sub-micrometer accuracy by quantitative analysis of the DHM phase images. As expected, due to the movement of the optical traps, an unequal deformation is observed in the first case (non-symmetric deformation), where the RBC was elongated along horizontal direction and it shrank slightly along the vertical one (Fig. 2c). In the second case (symmetric deformation) the RBC shrank and stretched along both directions (Fig. 2d). By calculating the ratio $R = h/v$ between horizontal

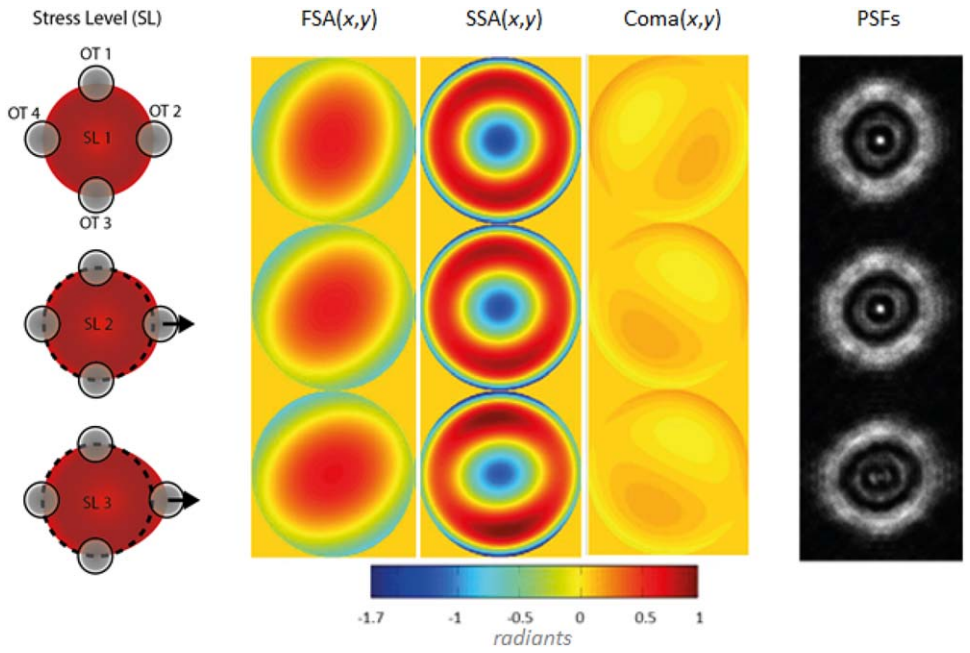

Figure 3. Aberrations and point spread functions (PSF) of the transmitted wavefront by a single RBC undergoing non-symmetric stretching. The three positions (or stress level, SL) are taken during deformation from Supporting Information Movie 1. [Color figure can be viewed at wileyonlinelibrary.com]

(h) and vertical (v) sizes of RBCs in Figure 2, we recover that R changes from 0.922 to 1.01 in the case of non-symmetric deformation (Fig. 2c), while it is stable at about 1.04 for symmetric deformation (Fig. 2d).

A more detailed morphological analysis of RBCs, during the deformation induced by HOTs, can be further performed by an image processing analysis (54). However, the main aim of our study is the investigation of the variation of RBC-focusing properties, when we consider the optically-deformed single RBC as a tunable adaptive optofluidic lens. For this purpose, the diffracted wavefronts at the exit pupil of the RBC-microlens, which are given by the corresponding QPM images, are expressed as a linear combination of Zernike polynomials (55,56):

$$\mathrm{QPM}(x,y) \approx \sum_{j=0}^{15} C_j Z_j(x,y) \tag{1}$$

where (x,y) are the spatial coordinates (pixels), C_j are the Zernike coefficients, and $Z_j(x,y)$ are the Zernike basis functions. Notice that we approximate the QPM image with the first 16 terms of the Zernike envelope, neglecting the larger orders. In addition, it has been demonstrated that main aberrations of a RBC-microlens are defocus and third-order spherical aberration, corresponding to the terms $j=4$ and $j=12$ in Eq. (1) (44). In the current work, we discover that the RBC deformations induced by HOTs correspond to remarkable variations of other aberrations, that is, astigmatism ($j=3$ and $j=5$), coma ($j=7$ and $j=8$), and secondary astigmatism ($j=11$ and $j=13$).

Thus, we rewrite Eq. (1) by modeling the QPM of a RBC with a sum of three terms:

$$\begin{aligned} &\mathrm{QPM}(x,y) \approx \mathrm{FSA}(x,y)+\mathrm{SSA}(x,y)+\mathrm{Coma}(x,y) \\ &\begin{cases} \mathrm{FSA}(x,y)=C_3Z_3(x,y)+C_4Z_4(x,y)+C_5Z_5(x,y) \\ \mathrm{SSA}(x,y)=C_{11}Z_{11}(x,y)+C_{12}Z_{12}(x,y)+C_{13}Z_{13}(x,y) \\ \mathrm{Coma}(x,y)=C_7Z_7(x,y)+C_8Z_8(x,y) \end{cases} \end{aligned} \tag{2}$$

where functions FSA(x,y) (Focus Shift and Astigmatisms) is the sum of focus shift and the two primary astigmatisms terms, SSA(x,y) (Spherical and Secondary Astigmatisms) is the sum of the third order spherical aberration and the two secondary astigmatisms terms, and Coma(x,y) is the sum of vertical and horizontal coma. These three functions take into account all morphological changes caused by RBC deformations. In particular FSA and SSA measure the focal properties variation of RBCs in terms of focal spots positions (39), calculated from only focus shift and third order spherical aberration terms, and their ellipticity, that is, primary and secondary astigmatisms. Thus, FSA and SSA correspond to the morphological variations of the convex and concave regions of the QPM, respectively.

In Figures 3 and 4 the aberrations of the wavefront during the asymmetric and the symmetric deformations, respectively, are reported. The aberrations correspond to the different level of stress that have been previously analyzed in Figure 2.

In particular, Figure 3 reports on the variation of FSA, SSA, and Coma, when only one of the four traps was moved along the horizontal axis. Notice that, before applying the stress (up row), FSA was affected by quasi vertical astigmatism, due to the initial ellipticity of the RBC's shape, measured from Figure 2c (i.e., $R=0.922$). Instead, the corresponding positive focal length, proportional to the maximum value of

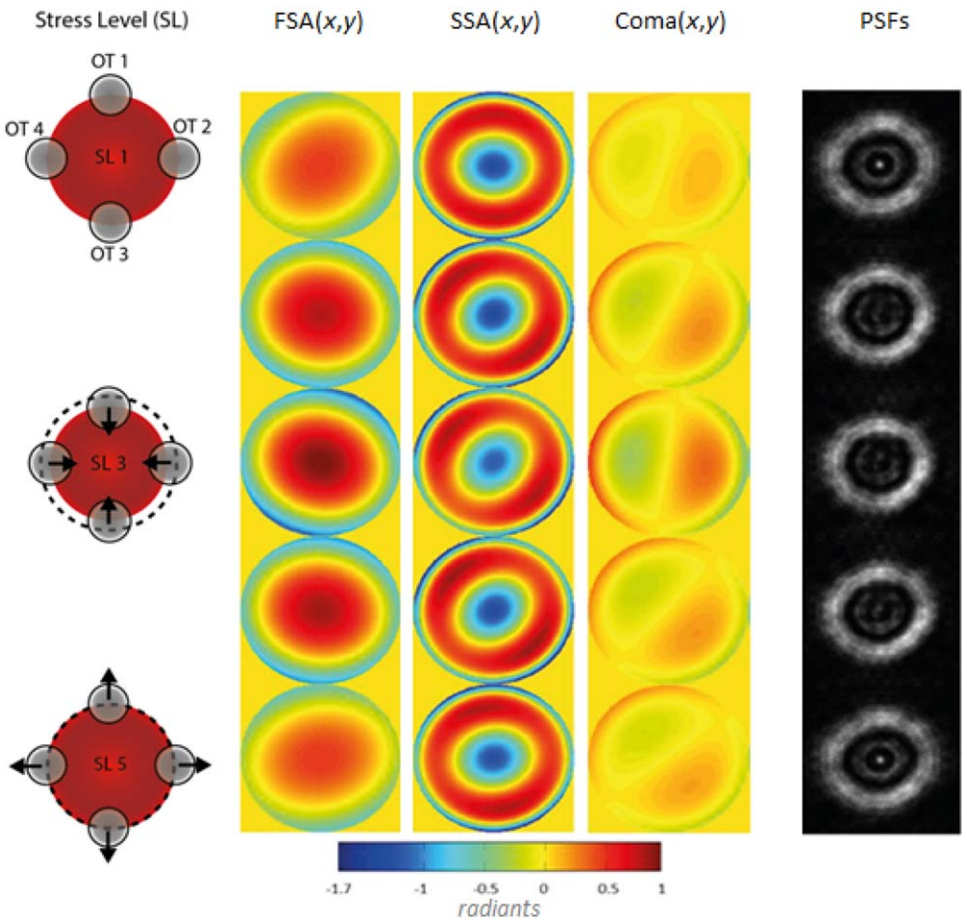

Figure 4. Phase maps, aberrations, and point spread functions of the transmitted wavefront during RBC shrinking and stretching. The five positions are taken during experiment from Supporting Information Movie 2. [Color figure can be viewed at wileyonlinelibrary.com]

this image FSA_{max}, was equal to 0.56 rad. After the stress application, we observe an overall reduction of the ellipticity and a rotation of such astigmatism up to about 45° (middle and bottom rows). In addition, no sensitive variations of the positive focal length is observed ($FSA_{max} = 0.58$ rad in the third row). Regarding SSA, we observe an initial near-zero secondary astigmatisms, measured by the ellipticity of the concave regions, while after stress a clearly visible elliptical concavity is observed, corresponding to the increasing of secondary astigmatisms. Concerning the negative focal length, proportional to the minimum value of SSA, it increased during the experiment, changing from $SSA_{min} = -1.53$ rad in the up row to $SSA_{min} = -1.17$ rad in the bottom row. For what concerns Coma, which generally arises when the source and the image are not perfectly aligned along the optical axis passing through the lens, it appeared with low intensity (see color scale of Fig. 3), with only angular variations during stretching. Finally, the last column of Figure 3 reports the point spread functions (PSFs) of the RBC-microlens during the experiment. Figure 4 reports the aberrations analysis in the case of symmetric stress. Here five RBC stress levels are shown, the starting one (no deformation), two for the compression and two for the stretching. As before, the phase maps were taken from a QPM time sequence (see Supporting Information Movie 2), in different instants of time. During the first steps the compression induced an increase on the positive focal length from $FSA_{max} = 0.46$ rad to $FSA_{max} = 0.99$ rad (see first and third rows respectively). Then during the stretching steps, the initial astigmatisms were almost recovered apart from a rotation of about 50°. At the same time we reveal a corresponding decrease of the negative focal length, from $SSA_{min} = -1.61$ to $SSA_{min} = -1.18$. This time, the Coma was present with higher intensity than in the case of a non-symmetrical deformation, but it was always weaker than other type of aberrations, reaching at maximum 0.5 rad (in absolute value). Overall, the subsequent two steps of stretching lead to restoration of the initial aberrations before stressing the RBC, where no deformations occurs (see fourth and fifth rows). This could open to the possibility of using HOTs to compensate/induce aberrations and/or change the focal length, that is, the corresponding imaging planes.

Conclusions

In summary, we exploited the RBC lens effect to analyze the wavefront transmitted by a healthy RBC under stretching with different HOTs configurations. Thanks to DH and Zernike polynomials analysis we have been able to precisely quantify the aberrations at different orders and so to characterize the "lens quality." Differently from other techniques, such as

that exploiting the saline buffer's variation, here we have the complete control on the lens deformation by HOTs, both for what concerns the "direction" of deformation and the speed. In particular, we deduced that the most relevant aberrations arising as consequence of cell deformation are the primary and secondary astigmatisms and the coma, while the focus shift and the third order spherical aberration can be manipulated to change the corresponding focal lengths.

Applications are foreseen in diagnostics: by studying the deformed wavefront, in fact, it is immediate to recover the elastic properties of a RBC, this giving information on its "healthiness," for example some blood diseases are related with a more rigid RBC's membrane. Moreover, from the biolens' aberration level (i.e., deformation) it could be possible to retrieve the age of a cell and/or the stored blood quality, by analyzing the different shape modification under the same stimulus, this being a critical parameter of storage lesion associated with complications in blood transfusions.

References

1. Gauvin F, Spinella PC, Lacroix J, Choker G, Ducruet T, Karam O, et al. Association between length of storage of transfused red blood cells and multiple organ dysfunction syndrome in pediatric intensive care patients. Transfusion 2010;50:1902–1913.
2. Hod EA, Brittenham GM, Billote GB, Francis RO, Ginzburg YZ, Hendrickson E, et al. Transfusion of human volunteers with older, stored red blood cells produces extravascular hemolysis and circulating non – transferrin-bound iron. Blood 2011; 118:6675–6682.
3. Zheng Y, Chen J, Cui T, Shehata N, Wang C, Sun Y. Characterization of red blood cell deformability change during blood storage. Lab Chip [Internet] 2014;14: 577–583.
4. Ciasca G, Papi M, Di Claudio S, Chiarpotto M, Palmieri V, Maulucci G, et al. Mapping viscoelastic properties of healthy and pathological red blood cells at the nanoscale level. Nanoscale R Soc Chem 2015;7:17030–17037.
5. Tomaiuolo G. Biomechanical properties of red blood cells in health and disease towards microfluidics. Biomicrofluidics 2014;8:10–19.
6. Gov N. Membrane undulations driven by force fluctuations of active proteins. Phys Rev Lett 2004;93:268104.
7. Shaked NT, Satterwhite LL, Telen MJ, Truskey GA, Wax A. Quantitative microscopy and nanoscopy of sickle red blood cells performed by wide field digital interferometry. J Biomed Opt 2011;16:030506–030503.
8. Pham HV, Bhaduri B, Tangella K, Best-Popescu C, Popescu G. Real time blood testing using quantitative phase imaging. Plos One 2013;8:e55676.
9. Lee GYH, Lim CT. Biomechanics approaches to studying human diseases. Trends Biotechnol 2007;25:111–118.
10. Guo Q, Reiling SJ, Rohrbach P, Ma H. Microfluidic biomechanical assay for red blood cells parasitized by Plasmodium falciparum. Lab Chip 2012;12:1143–1150.
11. Zheng Y, Nguyen J, Wang C, Sun Y. Electrical measurement of red blood cell deformability on a microfluidic device. Lab Chip 2013;13:3275–3283.
12. Henon Y, Sheard GJ, Fouras A. Erythrocyte deformation in a microfluidic cross-slot channel. RSC Adv R Soc Chem 2014;4:36079.
13. Tomaiuolo G, Lannote L, D'Apolito R, Cassinese A, Guido S. Microconfined flow behavior of red blood cells in vitro. Med Eng Phys J 2016;38:11–16.
14. Kuo F-J, Ho M-S, Dai J, Fan M-H. Atomic force microscopy for dynamic observation of human erythrocytes in a microfluidic system. RSC Adv R Soc Chem 2015;5: 101319–101326.
15. Haque MM, Moisescu MG, Valkai S, Dér A, Savopol T. Stretching of red blood cells using an electro-optics trap. Biomed Opt Express 2015;6:118.
16. Guck J, Ananthakrishnan R, Mahmood H, Moon TJ, Cunningham CC, Käs J. The optical stretcher: A novel laser tool to micromanipulate cells. Biophys J 2001;81:767–784.
17. Yoon Y-Z, Kotar J, Yoon G, Cicuta P. The nonlinear mechanical response of the red blood cell. Phys Biol 2008;5:036007.
18. Bambardekar K, Dharmadhikari AK, Dharmadhikari J. a, Mathur D, Sharma S. Measuring erythrocyte deformability with fluorescence, fluid forces, and optical trapping. J Biomed Opt 2014;13:064021.
19. Roth KB, Neeves KB, Squier J, Marr DWM. High-throughput linear optical stretcher for mechanical characterization of blood cells. Cytometry Part A 2016;89A:391–397.
20. Yang T, Bragheri F, Minzioni P. A comprehensive review of optical stretcher for cell mechanical characterization at single-cell level. Micromachines 2016;7:90.
21. Gu M, Kuriakose S, Gan X. A single beam near-field laser trap for optical stretching, folding and rotation of erythrocytes. Opt Express 2007;15:1369–1375.
22. Fedosov DA, Peltomäki M, Gompper G. Deformation and dynamics of red blood cells in flow through cylindrical microchannels. Soft Matter 2014;10:4258–4267.
23. Bareil PB, Sheng Y, Chen Y-Q, Chiou A. Calculation of spherical red blood cell deformation in a dual-beam optical stretcher. Opt Express 2007;15:16029–16034.
24. Merola F, Miccio L, Paturzo M, Finizio A, Grilli S, Ferraro P. Driving and analysis of micro-objects by digital holographic microscope in microfluidics. Opt Lett 2011;36: 3079–3081.
25. Zhang H, Liu K-K. Optical tweezers for single cells. J R Soc Interface [Internet] 2008; 5:671–690.
26. Stevenson DJ, Gunn-Moore F, Dholakia K. Light forces the pace: Optical manipulation for biophotonics. J Biomed Opt 2010;15:041503.
27. Lim CT, Dao M, Suresh S, Sow CH, Chew KT. Large deformation of living cells using laser traps. Acta Mater 2004;52:1837–1845.
28. Grier DG. A revolution in optical manipulation. Nature 2003;424:810–816.
29. Mejean CO, Schaefer AW, Millman E. a, Forscher P, Dufresne ER. Multiplexed force measurements on live cells with holographic optical tweezers. Opt Express 2009;17: 6209–6217.
30. Phillips DB, Grieve JA, Olof SN, Kocher SJ, Bowman R, Padgett MJ, et al. Surface imaging using holographic optical tweezers. Nanotechnology 2011;22:285503.
31. Olof SN, Grieve JA, Phillips DB, Rosenkranz H, Yallop ML, Miles MJ, et al. Measuring nanoscale forces with living probes. Nano Lett 2012;12:6018–6023.
32. Phillips DB, Padgett MJ, Hanna S, Ho Y-LD, Carberry DM, Miles MJ, et al. Shape-induced force fields in optical trapping. Nat Photon 2014;8:400–405.
33. Jayavanth S, Lee DH, Pak BC. Multi-shape erythrocyte deformability analysis by imaging technique. J Mech Sci Technol 2010;24:931–935.
34. Raj S, Marro M, Wojdyla M, Petrov D. Mechanochemistry of single red blood cells monitored using Raman tweezers. Biomed Opt Express 2012;3:753.
35. Kemper B, Kosmeier S, Langehanenberg P, von Bally G, Bredebusch I, Domschke W, et al. Integral refractive index determination of living suspension cells by multifocus digital holographic phase contrast microscopy. J Biomed Opt 2007;12:054009.
36. Rappaz B, Marquet P, Cuche E, Emery Y, Depeursinge C, Magistretti P. Measurement of the integral refractive index and dynamic cell morphometry of living cells with digital holographic microscopy. Opt Express 2005;13:9361–9373.
37. Przibilla S, Dartmann S, Vollmer A, Ketelhut S, Greve B, von Bally G, et al. Sensing dynamic cytoplasm refractive index changes of adherent cells with quantitative phase microscopy using incorporated microspheres as optical probes. J Biomed Opt 2012; 17:097001.
38. Memmolo P, Miccio L, Merola F, Gennari O, Netti PA, Ferraro P. 3D morphometry of red blood cells by digital holography. Cytometry Part A 2014;85A:1030–1036.
39. Seo KW, Byeon HJ, Lee SJ. Measuring the light scattering and orientation of a spheroidal particle using in-line holography. Opt Lett 2014;39:3915–3918.
40. Lee S-H, Grier DG. Holographic microscopy of holographically trapped three-dimensional structures. Opt Express 2007;15:1505–1512.
41. Daneshpanah M, Zwick S, Schaal F, Warber M, Javidi B, Osten W. 3D holographic imaging and trapping for non-invasive cell identification and tracking. IEEE/OSA J Disp Technol 2010;6:490–499.
42. Kemper B, Barroso Á, Woerdemann M, Dewenter L, Vollmer A, Schubert R, et al. Towards 3D modelling and imaging of infection scenarios at the single cell level using holographic optical tweezers and digital holographic microscopy. J Biophoton 2013;6:260–266.
43. Barroso Á, Woerdemann M, Vollmer A, Von Bally G, Kemper B, Denz C. Three-dimensional exploration and mechano-biophysical analysis of the inner structure of living cells. Small 2013;9:885–893.
44. Miccio L, Memmolo P, Merola F, Netti PA, Ferraro P. Red blood cell as an adaptive optofluidic microlens. Nat Commun 2015;6:6502.
45. Merola F, Paturzo M, Coppola S, Vespini V, Ferraro P. Self-patterning of a polydimethylsiloxane microlens array on functionalized substrates and characterization by digital holography. J Micromech Microeng 2009;19:125006.
46. Miccio L, Finizio A, Grilli S, Vespini V, Paturzo M, De Nicola S, Ferraro P. Tunable liquid microlens arrays in electrode-less configuration and their accurate characterization by interference microscopy. Opt Express 2009;17:2487.
47. Bowman RW, Gibson GM, Linnenberger A, Phillips DB, Grieve JA, Carberry DM, et al. Red tweezers: Fast, customisable hologram generation for optical tweezers. Comput Phys Commun 2014;185:268–273.
48. Kemper B, Vollmer A, Rommel CE, Schnekenburger J, von Bally G. Simplified approach for quantitative digital holographic phase contrast imaging of living cells. J Biomed Opt 2011;16:026014.
49. Memmolo P, Bianco V, Merola F, Miccio L, Paturzo M, Ferraro P. Breakthroughs in photonics 2013: Holographic imaging. IEEE Photon J 2014;6:0701106.
50. Merola F, Miccio L, Memmolo P, Paturzo M, Grilli S, Ferraro P. Simultaneous optical manipulation, 3-d tracking, and imaging of micro-objects by digital holography in microfluidics. IEEE Photon J 2012;4:451–454.
51. Kemper B, Langehanenberg P, Kosmeier S, Schlichthaber F, Remmersmann C, von Bally G, et al. Digital holographic microscopy: Quantitative phase imaging and applications in live cell analysis. In: Kemper B, editor. Handbook of Coherent-Domain Optical Methods. New York: Springer Science Business Media; 2013. 215 p.
52. Woerdemann M, Alpmann C, Denz C. Three-dimensional particle control by holographic optical tweezers. In: Wolfgang O, editor. Optical Imaging and Metrology: Advanced Technologies. New York: Wiley-VCH Verlag GmbH & Co. KGaA; 2012. p. 177–206.
53. Grover S, Gauthier R, Skirtach a. Analysis of the behaviour of erythrocytes in an optical trapping system. Opt Express 2000;7:533–539.
54. Yi F, Moon I, Javidi B. Cell morphology-based classification of red blood cells using holographic imaging informatics. Biomed Opt Express 2016;7:2385–2399.
55. Zernike F. Beugungstheorie des schneidenverfahrens und seiner verbesserten form, der phasenkontrastmethode. Physica 1934;1:689–704.
56. Malacara D, DeVore D. Interferogram evaluation and wavefront fitting. In: Malacara D, editor. Optical Shop Testing, 2nd ed. New York: Wiley Interscience; 1992. Chap. 13, pp. 455–495.